

Mg₂Si is the new black: introducing a black silicide with > 95% average absorption at 200-1800 nm wavelengths

Alexander Shevlyagin,^{1,*} Vladimir Il'yaschenko,¹ Aleksandr Kuchmizhak,^{1,2}
Eugeny Mitsai,¹ Alexander Sergeev,¹ Andrey Gerasimenko,³ and Anton Gutakovskii⁴

¹*Institute of Automation and Control Processes, Far Eastern Branch,
Russian Academy of Science, Vladivostok 690041, Russia*

²*Pacific Quantum Center, Far Eastern Federal University, 8 Sukhanova Str., Vladivostok, Russia*

³*Institute of Chemistry, FEB RAS, 690022, Vladivostok, Russia*

⁴*Institute of Semiconductor Physics of SB RAS, 630090, Novosibirsk, Russia*

Textured silicon surface structures, in particular black silicon (b-Si), open up possibilities for Si-based solar cells and photodetectors to be extremely thin and highly sensitive owing to perfect light-trapping and anti-reflection properties. However, near-infrared (NIR) performance of bare b-Si is limited by Si band gap of 1.12 eV or 1100 nm. This work reports a simple method to increase NIR absorption of b-Si by *in vacuo* silicidation with magnesium. Obtained Mg₂Si/b-Si heterostructure has a complex geometry where b-Si nanocones are covered by Mg₂Si shells and crowned with flake-like Mg₂Si hexagons. Mg₂Si formation atop b-Si resulted in 5-fold lower reflectivity and optical absorption to be no lower than 88% over 200-1800 nm spectral range. More importantly, Mg₂Si/b-Si heterostructure is more adjusted to match AM-1.5 solar spectrum with theoretically higher photogenerated current density. The maximal advantage is demonstrated in the NIR region compared to bare b-Si in full accordance with one's expectations about NIR sensitive narrow band gap (~ 0.75 eV) semiconductor with high absorption coefficient, which is Mg₂Si. Results of optical simulation confirmed the superiority of Mg₂Si/b-Si NIR performance. Therefore, this new wide-band optical absorber called black silicide proved rather competitive alongside state-of-the-art approaches to extend b-Si spectral blackness.

I. INTRODUCTION

Rigid semiconducting properties of the monocrystalline silicon (c-Si) place its single-junction solar cell (SC) efficiency to 29.4%¹ in accordance with Shockley-Queisser limit². Interdigitated back contact approach set a practical milestone of 26.7% in 2017³. Recently, bifacial Si SC pushed it to approximately 29% closing the gap between theory and experiment⁴. Simultaneously, a gradual thinning of Si wafers for reduction of the panel cost takes place. This search for a thinner light absorbing layer is additionally motivated by the much wider flexible SC applicability⁵⁻⁷. Therefore, modern Si SC industry has been narrowed down to the motto "thinner & cheaper" resulted in 10-fold decrease in thickness (20 μm)⁸ representing ultrathin SC niche and extremely thin ($< 3 \mu\text{m}$) freestanding SC beating 12% efficiency⁹. However, the thinner an absorbing layer, the lower short-circuit current density is generated, while generally decrease in Si wafer thickness results in its open-circuit voltage increase. A compromised thickness of 75 μm is believed to deliver a maximum photoelectric conversion efficiency of the Si SC¹⁰. In addition, absorbing performance can be enhanced by light-trapping effect allowing to maintain thin and ultrathin designs providing higher photogenerated current density in comparison with the flat absorbers¹¹.

Black silicon (b-Si) is a material of choice for the both thickness reduction below 100 μm toward flexible SC and light absorbing enhancement due to excellent trapping and antireflection properties¹². On the other hand, b-Si photovoltaic performance below Si band gap (1.12

eV or 1100 nm) leaves a room for the further improvements. The lower an incident photon energy, the lower optical losses and associated absorbance despite of multiple reflections in black structures. Thus, it is expected that near-infrared (NIR) absorbing layer deposited above b-Si surface would result in extension of its spectral blackness. So far, b-Si structures have been modified *via* thin film or nanoparticles deposition, formation of the hierarchical carbon-based nanostructures atop or pulsed laser postprocessing¹³⁻²¹. To date, practical use of the outlined approaches is limited by the low cost-efficiency factor resulted from the expensive deposition methods applied (atomic-layer deposition, molecular-beam epitaxy, *etc.*) and rare or high melting materials and compounds used (PtS₂, NbN, Au, TiN and MoS₂).

In this work, we propose a simple way to drastically increase b-Si NIR performance within thin coating of semiconducting (band gap ~ 0.75 eV²²) magnesium silicide (Mg₂Si) by vacuum evaporation technique. Mg₂Si is a Si-compatible optical material with superior absorbance from the ultraviolet (UV) to NIR regions compared to bare Si²³. It has already demonstrated photovoltaic perspectives as homo-/heterojunction photodetectors and SC²⁴⁻²⁹. Moreover, higher absorption coefficient exceeding 10⁵ cm⁻¹ above 1.5 eV²³ is favorable for Si wafer thinning confirmed by recent Mg₂Si/Si SC modeling³⁰. In addition, proposed route to cover b-Si with NIR absorbing material is simple, low temperature, scalable and fast method resulted from the benefits of vacuum evaporation.

We show that (*i*) vacuum evaporation results in b-Si geometry preservation and Mg₂Si flakes-like epitax-

ial growth atop b-Si nanocones, (ii) higher NIR performance is a result of both hierarchical Mg₂Si/b-Si structure and Mg₂Si intrinsic absorption, (iii) Mg₂Si coating resulted in only slight increase in UV-VIS reflection, while pronounced antireflection extends deeply below Si band gap down to that of Mg₂Si, and (iv) overall optical performance can be maximized through appropriate silicidation conditions. Optical modeling of the Mg₂Si/b-Si structure confirmed better localization of the NIR photons in comparison with uncovered b-Si. Finally, a survey on recent progress in b-Si modification in terms on NIR performance enhancement highlights new competitive black material with averaged over 200-1800 nm absorbance and reflectivity of 96% and 3.7%, respectively, called as black silicide.

II. EXPERIMENTAL DETAILS.

Black Si samples used as initial substrates for silicidation were produced *via* reactive-ion beam etching (RIE) as described elsewhere³¹. RIE with SF₆ and O₂ mixture was performed to produce the nanocones with average height and period of 200 and 100 nm, respectively, on Si(001) wafer.

Next, b-Si samples were cleaned by a standard wafer cleaning process with piranha solution for 10 minutes prior to vacuum chamber loading. For the silicidation of the b-Si a high vacuum turbomolecular pumped evaporation chamber with the base pressure of 1×10^{-6} Torr was used. The chamber is equipped with K-cell for Mg evaporation (5N, Alfa Aesar, USA), quartz crystal microbalance (QCM) sensor and rotating samples holder with resistive heater. QCM sensor was used for monitoring the deposition rate of Mg source. A calibration factor was obtained by comparing the thickness inferred from the QCM sensor with that of measured by atomic force microscopy on a specially step-shaped film deposited on bare Si(001) substrate. Before silicidation b-Si samples were degassed at 400 °C for 20 minutes under the pressure no worse than 8×10^{-5} Torr. A two-step growth technique known as solid phase epitaxy (SPE) was applied for Mg₂Si formation. First, 10-300 nm of Mg was deposited at room temperature with evaporation rate of 20 nm/min followed by sample annealing. The former resulted in metallic film formation on b-Si surface with pronounced light reflection contrasting to bare b-Si. It took about 5 minutes at 330-370 °C to obtain film color typical of Mg₂Si. During the SPE, vacuum pressure was no worse than 3×10^{-6} Torr. After the sample unloading from the chamber, its morphology, crystal structure, chemical composition and optical properties were investigated.

The X-ray diffraction (XRD) studies were carried out in the $2\theta/\omega$ mode and parallel beam optics geometry (RIGAKU SmartLab diffractometer, Japan). The XRD peaks were identified using the database ICDD PDF-2. Morphology of the Mg₂Si/b-Si (black silicide) surface

was characterized using scanning electron microscopy (SEM; Ultra 55+, Carl Zeiss, Germany). The crystal structure of prepared Mg₂Si/b-Si structure were studied by means of high resolution transmission electron microscopy (HRTEM, TITAN 80-300, FEI Company, USA) operated at 300 kV voltage with point-to-point resolution of 0.165 nm. The energy-dispersive X-ray spectroscopy (EDS) analysis was carried out in the cross-sectional STEM mode, with the electron beam size of ~ 1 nm. Raman scattering was pumped by a 473 nm CW laser using optical microscopy setup (NTEGRA Spectra II, NT-MDT, Russia) confocally aligned to a grating-type spectrometer with a thermo-electrically-cooled CCD-camera (i-Dus, Oxford Instruments, UK). The hemispheric total reflectance and transmittance for normal incidence in wavelength from 200 to 1800 nm were measured using a spectrophotometer with an integrating sphere (Cary 5000, Varian, USA). For comparison, reference spectra of bare b-Si were also obtained.

Finite-difference time-domain (FDTD) calculations have been carried out using commercial electromagnetic (EM) solver (Lumerical Solutions, Ansys Inc.). The morphology of the Mg₂Si/b-Si heterostructure was reproduced from the corresponding cross-sectional STEM image. Local EM field distributions were calculated for the black silicide and pure b-Si structures pumped under normal incidence at 1300 nm wavelengths. Complex dielectric function of the Mg₂Si was taken from Ref.²⁵.

III. RESULTS AND DISCUSSION.

A template substrate for black magnesium silicide preparation was fabricated via reactive ion etching of monocrystalline Si wafer with (001) surface orientation. This procedure resulted in well-known b-Si structure composed of the randomly distributed Si nanocones. Next, vacuum evaporation to cover b-Si surface with Mg₂Si layer was applied. Described protocol of the black silicide formation is illustrated in Fig.1a.

The as-loaded from vacuum chamber sample retains the typical nanocones structure of the bare b-Si shown in cross-sectional SEM images (Fig. 1b and c), whereas deposited Mg₂Si layer of the optimal thickness (see discussions below) is presented as flake-like faceted hexagons crowning b-Si edges (inset of Fig. 1c). The reflectance spectrum of the Mg₂Si covered b-Si nanocones array presented in Fig. 1d demonstrates strong NIR antireflection performance when compared to starting b-Si surface. These measurements confirm averaged reflection in the 200-1800 nm spectral range of 3.7% from black magnesium silicide surface, which is ~ 5 times lower with respect to 17.6% of the bare b-Si. However, the former material clearly demonstrates slightly increased VIS reflection with specific silicide related spectral feature at 500 nm (2.5 eV) resulted from first direct inter-band optical transition in Mg₂Si³². This fact suggests that Mg₂Si nanoflakes provide enough area for the sur-

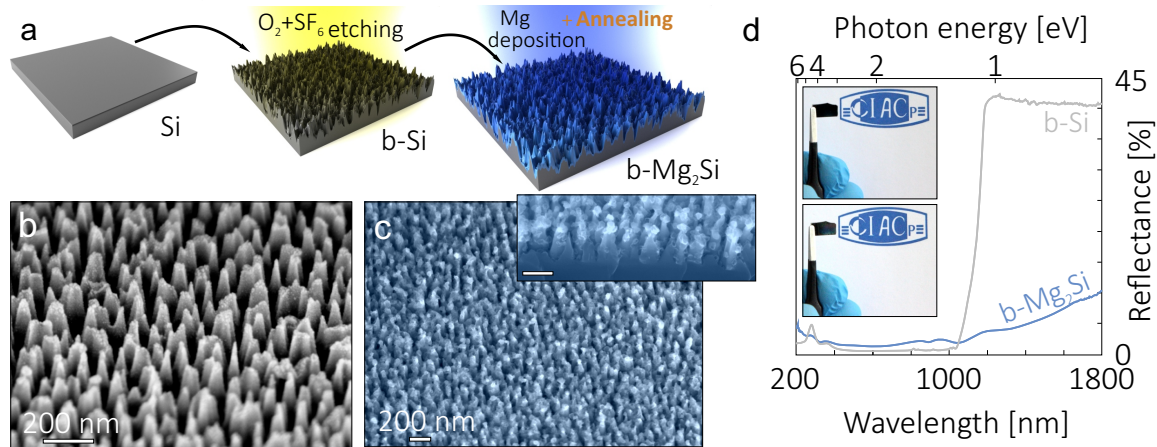


FIG. 1. Fabrication of the black magnesium silicide and its optical properties. (a) Schematic illustration of the $b\text{-Mg}_2\text{Si}$ preparation procedure. Side-view SEM images of the bare (b) and Mg_2Si (50 nm) covered (c) surface of the $b\text{-Si}$. Inset shows $b\text{-Si}$ nanocones crowned with flake-like Mg_2Si faceted hexagons. (d) Reflectance spectra of $b\text{-Mg}_2\text{Si}$ compared to bare $b\text{-Si}$. Insets show photographs of the as-prepared black silicide sample under different tilting angles.

face reflection being the main reason behind slight deterioration of the VIS antireflection. Insets on Figure 1d demonstrate photographs of $b\text{-Si}$ specimen after loading from vacuum evaporation chamber where silicidation took place. Grown $\text{Mg}_2\text{Si}/b\text{-Si}$ sample looks like uniform black surface to the naked eye. However, clear interface between bare (masked and uncovered with Mg_2Si layer) $b\text{-Si}$ area and Mg_2Si film appears while sample tilting. Moreover, Mg_2Si covering layer changes color from the black to deep blue intrinsic for silicide together with slightly higher VIS reflection further confirmed by optical measurements.

To illustrate the benefits of $b\text{-Si}$ with Mg_2Si layer in absorbing solar irradiance, optical transmittance (T) and reflectance (R) spectra were recorded from the ultraviolet (UV, 200 nm) to NIR (1800 nm) ranges (Figure 2a) and compared to state-of-the-art black surface structures^{13,14,16,20,33–35} (Figure 2c). Optical absorption spectra (A) calculated as $1-T-R$ demonstrate that optical properties of the $b\text{-Si}$ changed drastically after Mg_2Si deposition. In general, optical performance at $\lambda > 1100$ nm is significantly reduced in $b\text{-Si}$ structures, while black silicide structure can effectively absorb NIR light resulted from the smaller Mg_2Si band gap. Moreover, total reflection and absorption normalized to solar irradiance in accordance with expression:

$$R_{AM1.5G}^{norm}, A_{AM1.5G}^{norm} = \frac{\int_{\lambda=280nm}^{\lambda=1800nm} R(\lambda), A(\lambda) \times N(\lambda) d\lambda}{\int_{\lambda=280nm}^{\lambda=1800nm} N(\lambda) d\lambda}, \quad (1)$$

where $N(\lambda)$ is solar flux under AM1.5G illumination, allowed us to conclude that black silicide structure under consideration is superior to bare $b\text{-Si}$ in terms of NIR, overall and AM1.5G-normalized performance. Calculated values are summarized in Table 1.

Let us pay attention only to the most impressive results

obtained. For instance, black silicide structure demonstrates 6-fold decrease in NIR reflection being reduced from 38.5% down to 5.9% and 1.5 times higher NIR absorption. Moreover, $\text{Mg}_2\text{Si}/b\text{-Si}$ structure is better adjusted to match solar irradiance standard AM1.5G that reflected in 13-fold lower total reflection and higher averaged absorption of 97.5%. The latter allows to estimate the maximum achievable photo current density (MAPD) of the black silicide structure as:

$$J = \frac{eh}{C} \int_{\lambda=280nm}^{\lambda=1800nm} \lambda \times A(\lambda) \times N(\lambda) d\lambda, \quad (2)$$

where e , h , C and λ are electron charge, Planck constant, velocity of light and photon wavelength, respectively. MAPD reaches 54 mA/cm^2 under the assumption of recombination losses absent enhancing $b\text{-Si}$ MAPD by 3 mA/cm^2 . This claims black silicide as solar energy material with enhanced performance beyond 1100 nm.

Next, FDTD calculations were performed to study the effect of $b\text{-Si}$ covering with Mg_2Si layer. Figure 2b represents geometry of the grown $\text{Mg}_2\text{Si}/b\text{-Si}$ heterostructure reconstructed from the HAADF SEM data. The cross-sectional EM field distributions (E^2/E_0^2) near the surface of black silicide and bare $b\text{-Si}$ under illumination are presented in the bottom panels of Figure 2b. The wavelength 1300 nm was chosen to illustrate NIR performance enhancement associated with NIR absorbing Mg_2Si cover layer, while bare $b\text{-Si}$ can demonstrate marked IR absorption only under heavily doping and/or laser postprocessing^{21,35,36}. Thus, performed optical modeling clearly answers the question concerning increased NIR absorption taking place in black silicide structure. Higher EM field localization and hot spots are observed in the case of $\text{Mg}_2\text{Si}/b\text{-Si}$ structure with maximum confinement occurred near the $b\text{-Si}$ nanocones

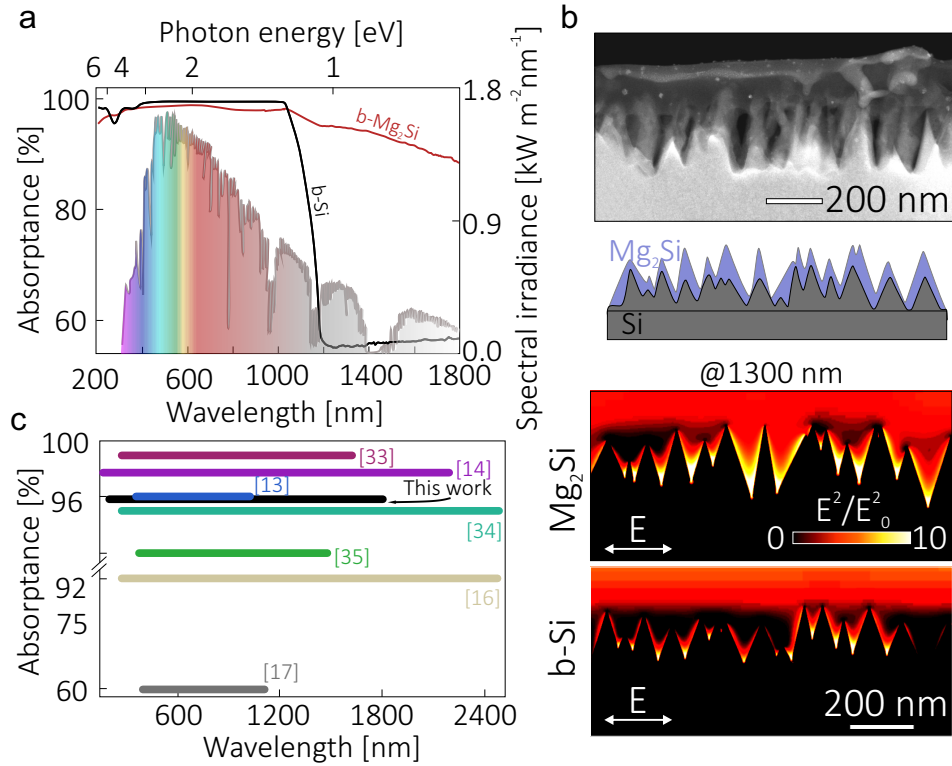


FIG. 2. Light absorbing properties of the black silicide in comparison with bare b-Si and other modified b-Si structures. (a) Absorbance spectra of the b-Mg₂Si and b-Si calculated from measured reflectance and transmittance with shown solar irradiance standard AM1.5G spectrum. (b) Black silicide morphology reconstruction basing on the STEM HAADF image for modeling normalized squared electric-field amplitude distribution (E^2/E_0^2) at 1300 nm pump wavelength of the Mg₂Si-covered and bare b-Si structures. (c) Survey of operating wavelength range and averaged optical absorption of the produced black silicide and several representative b-Si structures reported in^{13,14,16,20,33-35}.

TABLE I. Optical performance of the black silicide compared to bare black silicon including optical absorbance, reflectance averaged and normalized over different spectral ranges and photogenerated current densities under AM1.5G solar spectrum irradiance.

	R [200-1800 nm], %	R [1100-1800 nm], %	R AM1.5G, %	A [200-1800 nm], %	A [1100-1800 nm], %	A AM1.5G, %	MAPD, mA/cm ²
b-Si	17.56	38.56	29.8	81.1	58.3	92.1	50.9
b-Mg₂Si	3.66	5.87	2.3	95.8	92.8	97.5	54

base and Mg₂Si crowns. It can be tentatively concluded that complex hierarchical nanocones-nanoflake structure realized in black silicide resulted in the marked increase of the both NIR antireflection and absorption properties. NIR photons after being back-scattered within b-Si nanocones are effectively absorbed by Mg₂Si possessing much higher intrinsic absorption coefficient over wide spectral range.

Significantly, the wide range optical absorption performance of the black silicide is compared with state-of-the-art approaches to enhance NIR efficiency of the b-Si as shown in Fig. 2c. One can see that black silicide delivers absorption of $\sim 96\%$ over 200-1800 nm spectral range, while it does not require any expensive deposition methods and rare or high melting materials and compounds. For instance, PtS₂¹³ and NbN¹⁴ decorated b-Si with su-

perior absorption were produced under higher temperature budgets, while laser postprocessing of the b-Si often faces with Si amorphization^{20,37}, metastable phases formation and low minority carrier lifetime due to metal-like behavior after b-Si hyperdoping^{36,38,39}.

The second part of our work gives some insights into relation between b-Mg₂Si growth conditions and structural parameters as morphology, crystallinity and phase composition. On the other hand, these features strongly affect optical properties of the resulted nanostructures. Therefore, concerned markers were chosen to maximize wide-band antireflection and light absorbing performance of the black magnesium silicide.

Structural and elemental analysis of the black silicide sample are summarized in Figure 3a-d. The XRD pattern and Raman spectra shown in Fig. 3a and b, re-

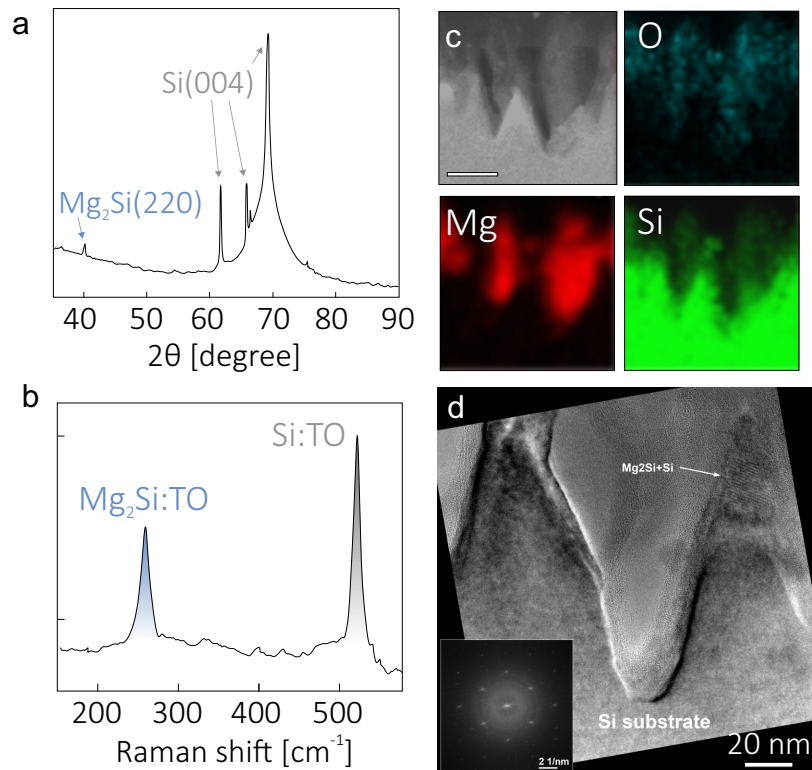


FIG. 3. Crystal structure and chemical composition of the prepared black silicide. (a) XRD pattern suggested (220) preferential orientation of the deposited Mg_2Si cover layer. (b) Representative Raman spectrum of the Mg_2Si sample showing TO phonon modes of crystalline Si and Mg_2Si . (c) Cross-sectional STEM-HAADF image and corresponding chemical elements composition mapping provided by EDS. (d) Representative cross-sectional HR-TEM image demonstrates refined morphology of the Mg_2Si deposits, which form core-shell Si- Mg_2Si complex nanostructure. Inset shows overall FFT pattern with reflexes corresponding to both Si and Mg_2Si .

spectively, suggest that *in vacuo* b-Si sample cleaning and silicidation at moderate temperature of the solid state reaction ($\sim 330^\circ\text{C}$) have no influence on b-Si intrinsic properties. XRD and Raman peak positions coincide well with bulk Si and no signs of amorphization are observed. It makes sense in terms of the well-known antireflection properties degradation of the RIE derived b-Si after thermal annealing⁴⁰. Neither metastable Mg-silicide phases, nor magnesium oxides, hydrates and silicates can be seen regardless low vacuum conditions. In addition, grown Mg_2Si layer demonstrates good crystallinity resulting in (i) only (220) diffraction peak appearance corresponded to Mg_2Si with $\text{Fm}\bar{3}\bar{m}$ crystal lattice and (ii) pronounced TO phonon mode observation with intensity comparable to that of Si, despite thin silicide film deposition. The former suggests that the grown Mg_2Si shells have preferential orientation on the b-Si nanocones. Mg_2Si crystallites mean size and residual stress were calculated to be 28 nm and 0.2%, respectively in accordance with XRD data. Thus, Mg_2Si cover layer does not disgrace the best ultrahigh vacuum grown Mg_2Si films in terms of crystallinity, whereas much lower vacuum and substrate surface treatment requirements were used^{22,29,41–43}. These facts confirm high applicability and scalability degrees of the proposed new

black material preparation. HAADF-STEM imaging and EDS elemental mapping (Fig. 3c) have been carried out to illustrate Mg_2Si /b-Si morphology and chemical composition. These findings confirm that Mg_2Si /b-Si sample is a stacked textured structure with Mg_2Si layer repeating b-Si nanocones geometry to some extent. Elemental oxygen is related to atmosphere long-term exposure. A closer look at the individual b-Si nanocones covered with Mg_2Si is shown in the HRTEM image (Figure 3d). Magnesium silicide is presented with few-nm thick crystalline shell surrounding b-Si nanocones with well-defined reflexes on FFT inset. Thus, Mg_2Si /b-Si material is a hierarchically organized nanostructure where b-Si nanocones are covered with thin Mg_2Si shells and crowned by Mg_2Si nanoflakes.

To find the optimal conditions for Mg_2Si growth atop b-Si, Mg_2Si /b-Si samples crystallinity, morphology, phase composition and optical properties were investigated depending on deposited Mg film thickness and substrate temperature upon solid phase epitaxy. The former varied from 10 to 300 nm and the latter did in 250–450 °C temperature range.

When fixing SPE temperature slightly above 300 °C, which is favorable for magnetron sputtering and thermal evaporation of Mg_2Si films on Si substrates^{26,44–46},

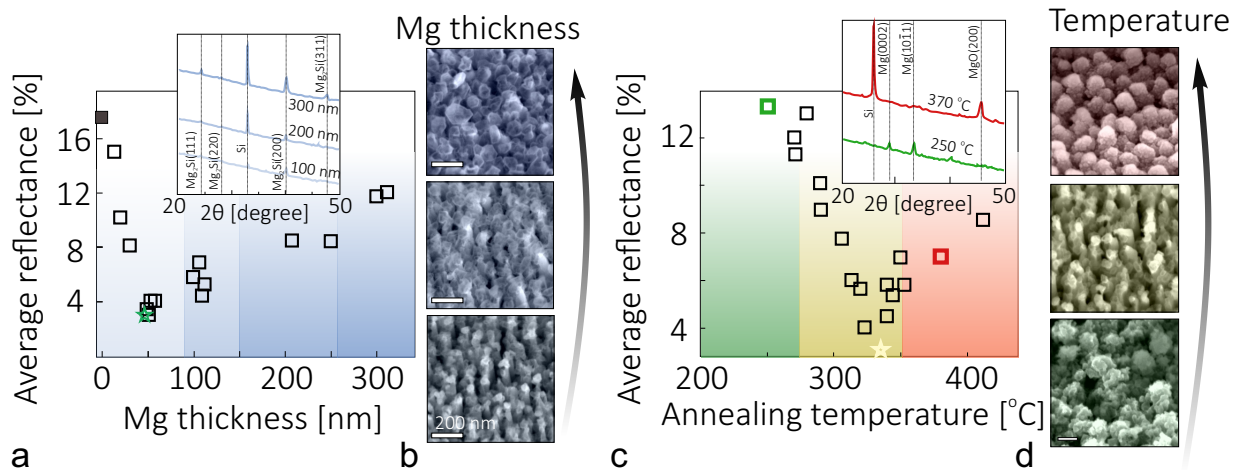


FIG. 4. Summary of the optimal Mg film thickness (a, b) and annealing temperature (c, d) findings for boosting NIR antireflection performance of the proposed black magnesium silicide. SEM (b, d) and XRD (insets of a, c) investigations served as morphology and phase composition markers, which have crucial influence on the optical properties. Left panels (a, b) represent samples annealed under the same SPE conditions ($\sim 330^\circ\text{C}$), while the right ones (c, d) do that of under the constant Mg film thickness of ~ 50 nm.

resulting coated b-Si nanostructures demonstrate non monotonic antireflection behavior (defined as averaged on 200-1800 nm optical reflectance) with increase in Mg layer thickness (see Fig. 4a, main frame). First, one can see an abrupt decrease in reflection as Mg thickness approaches 50 nm being a global minimum with the best antireflection performance. Representative morphology evolution of the Mg₂Si/b-Si heterostructures is shown in series of the cross-sectional SEM images in Fig. 4b. Passing global minimum of the Mg₂Si/b-Si reflectance, the thicker deposited Mg film, the lower antireflection is demonstrated. This tendency resulted from Mg₂Si nanoflakes enlargement and increase in surface reflection from it. At higher thickness almost continuous Mg₂Si film is observed. In addition, Mg₂Si nanoflakes enlargement resulted in higher intensity of the main Mg₂Si (220) and other (200), (111) and (311) diffraction peaks appearance suggested polycrystalline Mg₂Si growth atop b-Si nanocones (inset of Fig. 4a). As a result, thin Mg films of about 50 nm in thickness are of interest in terms of the best antireflection properties. It corresponds to formation of a complex Mg₂Si/b-Si nanostructures upon SPE annealing, which preserves b-Si light-trapping geometry extending its spectral blackness.

At the second stage, effect of the SPE temperature on the average reflectivity of the Mg₂Si/b-Si was examined for the fixed 50-nm thick Mg film thickness determined previously as optimal. The data are summarized in Fig. 4c showing that minimal reflectance is achieved at $\sim 330^\circ\text{C}$. Interestingly, temperature below 270°C is not enough for complete silicidation of the b-Si nanocones. XRD data (inset of Fig. 4c) clearly demonstrate contribution from metallic hexagonal Mg with (0002) and (10 $\bar{1}$ 1) reflexes. In contrast, when an-

nealing temperature exceeds 370°C , low vacuum condition used resulted in Mg oxidation rather than silicide formation. It reflects in diffraction from (200) crystal plane of the cubic MgO plane and absence of any Mg₂Si related phonon modes in Raman measurements. In addition, in both cases the surface morphology changed to popcorn like structure (Figure 4d) resulting in increase of the total reflectance. Therefore, low temperature ($\sim 330^\circ\text{C}$) solid phase epitaxy of the thin (~ 50 nm) Mg film atop b-Si structure are both required to modify its optical properties toward NIR blackness.

IV. CONCLUSION

In summary, a simple and low-cost method for boosting NIR absorption performance of black silicon by integrating with magnesium silicide is demonstrated. Resulting Mg₂Si/b-Si heterostructure preserves antireflection and light-trapping properties of the b-Si associated with nanocones-like geometry and expands its spectral blackness from 1100 nm to at least 1800 nm owing to NIR sensitive narrow-band-gap Mg₂Si cover layer. Explored and verified by modeling optical properties of this new wide-band black material called black silicide suggest some possible applications ranging from NIR optical absorbers, high-sensitive NIR devices and solar cells. Results obtained propose material scientists, especially dealing with Si-silicide tandem solar cells engineering, a simple technology to enhance photoelectric conversion efficiency using a b-Si as a platform for silicidation with other environment-friendly and Si-compatible silicides, for example BaSi₂ or β -FeSi₂.

V. DECLARATION OF COMPETING INTEREST

The authors declare that they have no known competing financial interests or personal relationships that could have appeared to influence the work reported in this paper.

VI. ACKNOWLEDGEMENTS

This research was supported by the Russian Science Foundation under Grant No. 20-72-00006. Authors are

thankful to Prof. Saulius Juodkakis from Optical Sciences Centre and ARC Training Centre in Surface Engineering for Advanced Materials, School of Science, Swinburne University of Technology for providing bare black Si samples.

VII. REFERENCES

-
- * shevlyagin@iacp.dvo.ru
- ¹ B. A. Veith-Wolf, S. Schäfer, R. Brendel, and J. Schmidt, *Solar Energy Materials and Solar Cells* **186**, 194 (2018).
 - ² W. Shockley and H. J. Queisser, *Journal of applied physics* **32**, 510 (1961).
 - ³ K. Yoshikawa, H. Kawasaki, W. Yoshida, T. Irie, K. Konishi, K. Nakano, T. Uto, D. Adachi, M. Kanematsu, H. Uzu, *et al.*, *Nature energy* **2**, 1 (2017).
 - ⁴ “<https://www.anu.edu.au/news/all-news/anu-scientists-set-new-record-with-bifacial-solar-cells>, accessed: May, 2022,” .
 - ⁵ S. A. Hashemi, S. Ramakrishna, and A. G. Aberle, *Energy & Environmental Science* **13**, 685 (2020).
 - ⁶ H.-D. Um, I. Hwang, D. Choi, and K. Seo, *Accounts of Materials Research* **2**, 701 (2021).
 - ⁷ J. Zhao, J. Zha, Z. Zeng, and C. Tan, *Journal of Materials Chemistry A* (2021).
 - ⁸ I. Massiot, A. Cattoni, and S. Collin, *Nature Energy* **5**, 959 (2020).
 - ⁹ M. Xue, K. N. Nazif, Z. Lyu, J. Jiang, C.-Y. Lu, N. Lee, K. Zang, Y. Chen, T. Zheng, T. I. Kamins, *et al.*, *Nano Energy* **70**, 104466 (2020).
 - ¹⁰ U. Chime, L. Wolf, V. Buga, D. Weigand, A. Gad, J. Köhler, A. Lambertz, W. Duan, K. Ding, T. Merdzhanova, *et al.*, *Solar RRL* **6**, 2100594 (2022).
 - ¹¹ R. Saive, *Progress in Photovoltaics: Research and Applications* **29**, 1125 (2021).
 - ¹² M. Otto, M. Algasinger, H. Branz, B. Gesemann, T. Gimpel, K. Fücksel, T. Käsebieber, S. Kontermann, S. Koynov, X. Li, *et al.*, *Advanced optical materials* **3**, 147 (2015).
 - ¹³ J. Lu, W. Zhuang, W. Yang, X. Zhang, G. Su, X. Gong, J. Yuan, J. Sui, Y. Zhou, G. Zhang, *et al.*, *The Journal of Physical Chemistry C* **125**, 27335 (2021).
 - ¹⁴ K. Isakov, A. P. Perros, A. Shah, and H. Lipsanen, *Nanotechnology* **29**, 335303 (2018).
 - ¹⁵ Y. Song, T. Liu, S. Liu, J. Huang, J. Li, C. Tian, T. Yu, Y. He, Y. Liu, and Z. Zhong, *Journal of Materials Science: Materials in Electronics* **31**, 4696 (2020).
 - ¹⁶ K. Wang, S. Liu, J. Li, S. Wu, J. Xia, J. Chen, C. Tian, Y. Liu, and Z. Zhong, *Journal of Materials Science: Materials in Electronics* **32**, 11503 (2021).
 - ¹⁷ A. Sarkar, S. Mukherjee, A. K. Das, and S. K. Ray, *Nanotechnology* **30**, 485202 (2019).
 - ¹⁸ A. Shah, P. Stenberg, L. Karvonen, R. Ali, S. Honkanen, H. Lipsanen, N. Peyghambarian, M. Kuitinen, Y. Svirko, and T. Kaplas, *Scientific reports* **6**, 1 (2016).
 - ¹⁹ T. L. Phan and W. J. Yu, *Scientific reports* **10**, 1 (2020).
 - ²⁰ M. I. Sánchez, P. Delaporte, Y. Spiegel, B. Franta, E. Mazur, and T. Sarnet, *physica status solidi (a)* **218**, 2000550 (2021).
 - ²¹ S. Paulus, P. Mc Kearney, F. Völklein, and S. Kontermann, *AIP Advances* **11**, 075014 (2021).
 - ²² J. E. Mahan, A. Vantomme, G. Langouche, and J. P. Becker, *Physical Review B* **54**, 16965 (1996).
 - ²³ T. Kato, Y. Sago, and H. Fujiwara, *Journal of Applied Physics* **110**, 063723 (2011).
 - ²⁴ A. A. El-Amir, T. Ohsawa, T. Nabatame, A. Ohi, Y. Wada, M. Nakamura, X. Fu, K. Shimamura, and N. Ohashi, *Materials Science in Semiconductor Processing* **91**, 222 (2019).
 - ²⁵ H. Udono, H. Tajima, M. Uchikoshi, and M. Itakura, *Japanese Journal of Applied Physics* **54**, 07JB06 (2015).
 - ²⁶ A. A. El-Amir, T. Ohsawa, S. Ishii, M. Imura, M. Liao, X. Fu, H. Segawa, I. Sakaguchi, T. Nagao, K. Shimamura, *et al.*, *Materials Science in Semiconductor Processing* **102**, 104577 (2019).
 - ²⁷ Q. Zhu, P. Ye, Y. Tang, X. Zhu, Z. Cheng, J. Xu, and M. Xu, *Nanotechnology* **33**, 115202 (2021).
 - ²⁸ H. Yu, L. Sun, S. Ji, R. Deng, Z. Mo, and Q. Xie, *IEEE Photonics Journal* **14**, 1 (2021).
 - ²⁹ A. Shevlyagin, I. Chernev, N. Galkin, A. Gerasimenko, A. Gutakovskii, H. Hoshida, Y. Terai, N. Nishikawa, and K. Ohdaira, *Solar Energy* **211**, 383 (2020).
 - ³⁰ Q. Deng, Z. Wang, S. Wang, and G. Shao, *Solar Energy* **158**, 654 (2017).
 - ³¹ E. P. Ivanova, J. Hasan, H. K. Webb, G. Gervinskas, S. Juodkakis, V. K. Truong, A. H. Wu, R. N. Lamb, V. A. Baulin, G. S. Watson, *et al.*, *Nature communications* **4**, 1 (2013).
 - ³² M. Au-Yang and M. L. Cohen, *Physical Review* **178**, 1358 (1969).
 - ³³ T. P. Pasanen, J. Isometsä, M. Garin, K. Chen, V. Vähänissi, and H. Savin, *Advanced Optical Materials* **8**, 2000047 (2020).
 - ³⁴ H. Zhong, A. Guo, G. Guo, W. Li, and Y. Jiang, *Nanoscale research letters* **11**, 1 (2016).
 - ³⁵ M. A. Sheehy, B. R. Tull, C. M. Friend, and E. Mazur, *Materials Science and Engineering: B* **137**, 289 (2007).
 - ³⁶ M.-J. Sher, C. B. Simmons, J. J. Krich, A. J. Akey, M. T. Winkler, D. Recht, T. Buonassisi, M. J. Aziz, and A. M.

- Lindenberg, Applied Physics Letters **105**, 053905 (2014).
- ³⁷ Y. Borodaenko, S. Syubaev, S. Gurbatov, A. Zhizhchenko, A. Porfirev, S. Khonina, E. Mitsai, A. V. Gerasimenko, A. Shevlyagin, E. Modin, *et al.*, ACS Applied Materials & Interfaces **13**, 54551 (2021).
- ³⁸ M. T. Winkler, D. Recht, M.-J. Sher, A. J. Said, E. Mazur, and M. J. Aziz, Physical Review Letters **106**, 178701 (2011).
- ³⁹ J. Sickel, A. Ahrens, A. Baumann, W. Schade, S. Kontermann, and M. Seibt, *physica status solidi (a)* **214**, 1700264 (2017).
- ⁴⁰ C. H. Crouch, J. Carey, M. Shen, E. Mazur, and F. Genin, Applied Physics A **79**, 1635 (2004).
- ⁴¹ A. Vantomme, J. E. Mahan, G. Langouche, J. P. Becker, M. Van Bael, K. Temst, and C. Van Haesendonck, Applied physics letters **70**, 1086 (1997).
- ⁴² A. Gournalnik, A. Maslov, A. Y. Ustinov, S. Dotsenko, A. Shevlyagin, I. Chernev, V. Il'yashenko, S. Kitan, E. Koblova, K. Galkin, *et al.*, Applied Surface Science **439**, 282 (2018).
- ⁴³ A. S. Gournalnik, A. V. Shevlyagin, I. M. Chernev, A. Y. Ustinov, A. V. Gerasimenko, and A. K. Gutakovskii, Materials Chemistry and Physics **258**, 123903 (2021).
- ⁴⁴ H. Yu, Q. Xie, and Q. Chen, Journal of Materials Science: Materials in Electronics **24**, 3768 (2013).
- ⁴⁵ A. Katagiri, S. Ogawa, M. Uehara, P. Sankara Rama Krishnan, M. Kurokawa, M. Matsushima, T. Shimizu, K. Akiyama, and H. Funakubo, Journal of materials science **53**, 5151 (2018).
- ⁴⁶ B. Zhang, T. Zheng, Q. Wang, Y. Zhu, H. N. Alshareef, M. J. Kim, and B. E. Gnade, Journal of Alloys and Compounds **699**, 1134 (2017).